NUCL SCI TECH (2020) 31:40
https://doi.org/10.1007/s41365-020-0743-7

A noninvasive Ionization Profile Monitor for transverse beam cooling and orbit oscillation study in HIRFL-CSR

Hong-Ming Xie[1] · Ke-Wei Gu[1] · Yuan Wei[1,2] · Yong Zhang[1] · Guang-Yu Zhu[1] · Long Jing[1,2] · Zhi-Xue Li[1] · Li-Li Li[1] · Xue-Jing Hu[1] · Li-Jun Mao[1] · Ze Du[1] · Jun-Xia Wu[1]

Received: 1 November 2019 / Revised: 13 February 2020 / Accepted: 16 February 2020 / Published online: 19 March 2020

Abstract A noninvasive Ionization profile monitor (IPM) consisting of micro-channel plates, a phosphor screen and the optical-signal acquisition has been developed at the cooling storage ring of Heavy Ion Research Facility in Lanzhou (HIRFL-CSR). It makes the real-time profile measurements for the transverse beam cooling and orbit oscillation possible and efficient. This paper firstly describes all the IPM design criterions including the theoretical signal yield calculation, the space charge field and initial momentum evaluation, and the electrostatic field distortion simulation as well. In order to investigate the IPM performance, the beam profile measurements are done with different high voltage settings. Subsequently, some valuable beam experiments about the transverse electron cooling and orbit oscillation study are also presented. In the end, fast turn-by-turn profile measurements for the emittance blow-up research in a synchrotron are discussed. In cooperation with the newly deployed emittance instruments at the HIRFL-CSR injector, the IPM shows great prospects for the injection mismatch study, and potential values for the tune, dispersion and chromaticity measurements as well.

Keywords IPM · Beam profile · Electron cooling · Transverse emittance · Orbit oscillation · Injection mismatch

This work was supported by the National Natural Science Foundation of China (No. 11805250).

✉ Ze Du
duze@impcas.ac.cn

✉ Jun-Xia Wu
wujx@impcas.ac.cn

Hong-Ming Xie
xiehongm@impcas.ac.cn

1 Institute of Modern Physics, Chinese Academy of Sciences, Lanzhou 730000, China

2 University of Chinese Academy of Sciences, Beijing 100049, China

1 Introduction

Heavy Ion Research Facility in Lanzhou (HIRFL) [1] is a multi-functional cooling storage ring system, which consists of a main ring (CSRm), an experimental ring (CSRe), and a radioactive isotope beam line (RIBLL2) to connect the two rings. Figure 1 shows the layout of the accelerator complex with colored marks representing the IPMs and electron coolers. Previously, a scintillator screen is deployed for the beam profile diagnostics at CSRm, which is a traditional interceptive method that cannot be used during the beam normal operation. Therefore, a non-intercepting instrument is urgently needed for the real-time profile monitoring in HIRFL-CSR.

As one of the most valuable noninvasive profile instruments for the proton and heavy ion facility, the working principle of Ionization profile monitor (IPM) can be summarized as follows. Firstly, a certain number of ionization products (gas ions or electrons) originate from the Coulomb interaction between the beam particles and residual gas molecules. And they are accelerated to the detector chip by a strong electrostatic field perpendicular to the beam propagation direction. Such an electric field should be designed as uniform as possible to drive the signal particles performing an undistorted drift motion.

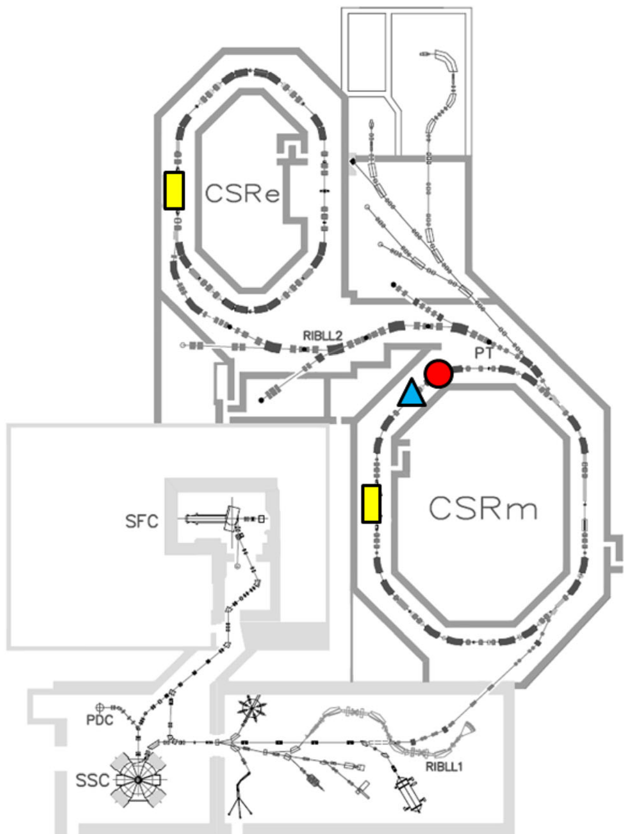

Fig. 1 (Color online) The layout of HIRFL complex, in which the yellow rectangles represent the electron coolers in CSR, and the red circle and blue triangle are the vertical and new horizontal IPMs

Eventually, the detected signals are positively proportional to the density of the beam particles, so the real profile distribution can be retrieved.

According to the signal collection species (residual gas ion or electron collection) and signal readout technologies (electrical or optical signal acquisition), IPMs are usually classified into several types [2]. Generally, the electron collection is chosen for the advantage of shorter drift time compared to the gas ion collection, whereas the profile measurement accuracy can be negatively affected by the space charge field from intense beams, and the large initial velocity of signal electrons as well. As a result, the fast IPMs are usually equipped with a dipolar magnetic field parallel to the electric field so as to force the signal electrons performing a helical motion.

As for the signal acquisition techniques, an expensive way by the multi-channel electronics acquisition can achieve a fast response frequency up to above 1 MHz bandwidth, but it also causes a relatively poor spatial resolution around 1 mm due to the anode size limitation. In contrast, the optical signal acquisition with a phosphor screen can realize a high spatial resolution up to tens of microns, while it brings a slow response time due to the frame rate limits of the camera used.

Presently, one popular type of IPM is constructed with the electron collection and the multi-channel electronics readout for a fast profile measurement, like the turn-by-turn profile diagnostics in a synchrotron. In view of the small beam size after the electron cooling in HIRFL-CSRm, another common structure of IPM comprising micro-channel plates (MCPs), a phosphor screen P46 and the camera acquisition turns into our practical choice eventually. In fact, the IPM classification is becoming more and more ambiguous and meaningless with the development of new detection technologies, such as the hybrid pixel detector [3].

Taking advantage of the ionization products, an IPM can only measure the one-dimensional distribution of transverse beams (vertical or horizontal profile). Since the first vertical IPM was installed at HIRFL-CSRm in 2016 [4], it had played an important role at every stage of providing beams. During the summer maintenance in 2018, a new horizontal IPM with a superior mechanical design and an upgraded control system was developed. In the thesis, all of the major design issues, stimulation of performances and beam experiments about the new IPM are described step by step in Sect. 2. And the applications and future prospects of such a noninvasive profile instrument are subsequently discussed from Sects. 3 to 5.

2 New IPM design and upgrades

2.1 Mechanical design and control system upgrades

The upper panel of Fig. 2 shows the mechanical design of the vertical (left picture) and new horizontal (right picture) IPMs. Obviously, a few mechanical features and changes are listed as follows.

- The clearance between the upper and lower plates is approximately 170 mm in the vertical IPM, while it is compactly designed only 120 mm for the new IPM. Undoubtedly, a shorter clearance will result in less time used for the signal ions' drift and consequently higher profile measurement accuracy. In case of blocking the beams, this dimension can only be properly reduced to a certain extent.
- The number of the bias electrodes is 18 in the vertical IPM for the field shaping, but it is designed only 8 for the new IPM due to a larger surface of each electrode parallel to the electric field direction. This change is beneficial not only to reduce the number of the bias electrodes needed, but also to maintain the uniformity of the electric field.

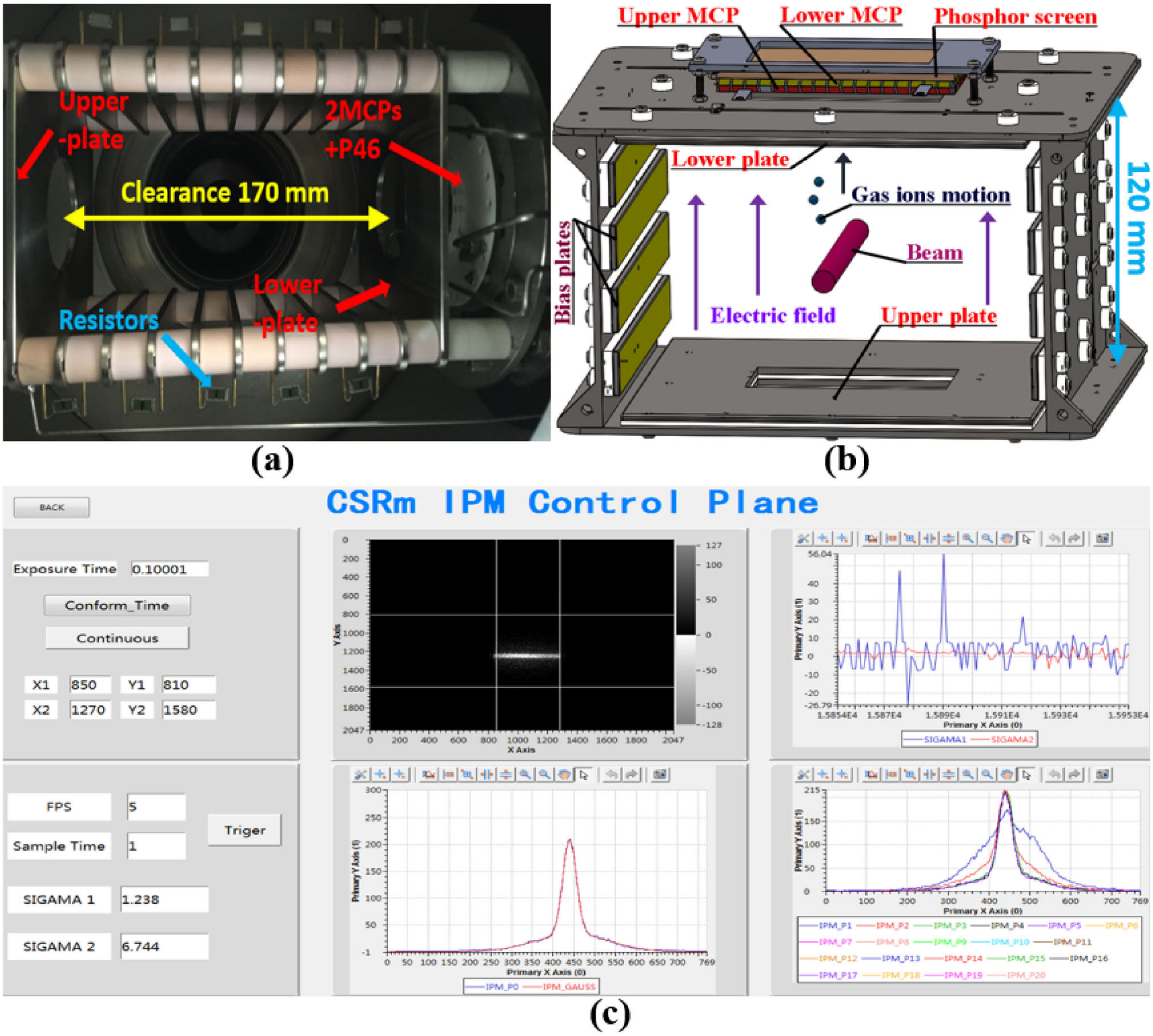

Fig. 2 (Color online) The IPM sketch and control system, in which the panel **a** shows the vertical IPM with some 100 mega-ohm resistors for the field shaping, **b** is the new compact design of horizontal IPM with separate HV supplies, and **c** is an EPICS control system showing the raw image of beams and the processed profile data

- Instead of circular MCPs applied in the former vertical IPM, the new IPM uses rectangular MCPs for the advantage of a larger effective area. In addition, the insulator material of MCPs relating to the thermal baking and the vacuum outgassing should be carefully chosen.
- To avoid the possible resistors deterioration during a harsh thermal baking, the new IPM uses separate electrodes for each bias voltage supply rather than by means of the tandem resistors. This change will surely increase the costs of HV channels, but it makes the voltage values on each of the IPM electrodes controllable and precise.

Some delicate material and surface treatments are demanded during the new IPM manufacture. At first, the 316L type stainless steel and the 99% aluminum oxide ceramic are both pre-treated inside a 900 degree Celsius furnace for the surface outgassing. Then in order to prevent some microscopic protuberances discharging, all the metallic electrodes are carefully processed by the ultrasonic cleaning, the surface polishing, and the edge grinding as well. Moreover, all the connection points between the insulator ceramic and metallic electrodes are carefully designed to avoid any surface discontinuity, which is especially important on the inner surface of the bias electrodes to form a uniform electric field.

The optics system is simply designed by setting the camera directly after a quartz view window for a large numerical aperture. As for the high radiation case, an optical fiber or a long-distance reflective light path may be needed for the sake of the camera protection. Generally, the spatial uncertainty from the two-layer MCPs is approximately 3 times the pore spacing of 12 μm, thus the spatial resolution of the whole optics system calibrated around 63 μm per pixel seems convincing and reliable. A 4.2 mega-pixel scientific complementary metal–oxide–semiconductor (sCMOS) chip is connected with two camera link (CL) cables for the digital data transmission. The response frequency of this sCMOS camera has been tested up to 100 frames per second with the full pixel resolution.

The former IPM utilizes a commercial software to control the camera with no data processing function. As shown in the lower panel of Fig. 2, a new IPM control system has been developed based on the Experimental Physics and Industrial Control System (EPICS), which easily accomplishes many useful features including the Region Of Interest (ROI) selection, the profile data fitting and the historical profile display, etc. It also can be triggered by a nearby DC current transformer (DCCT) to simultaneously store the transverse profile and beam current data. The whole system eventually achieves approximately 200 ms time delay with the exception of the camera exposure time, which is much slower than the camera response time of 10 ms. This is mainly because of the profile data processed via the EPICS Process Variables (PVs), and a faster way is to process the massive image data by a field-programmable gate array (FPGA) hardware.

2.2 Initial signal yield evaluation

An evaluation about the initial signal yield is essential for the IPM design, especially for the application cases under the ultra-high vacuum condition in a synchrotron. In theory, the Coulomb collision mostly occurs between the charged beam particles and the orbit electrons of residual gas molecules; thus, the energy loss also can be regarded as the electric stopping power in gas targets. The electric stopping power can be described by the well-known Bethe formula in Eq. (1) [5].

$$-\frac{\mathrm{d}E}{\mathrm{d}x} = 4\pi N_\mathrm{A}\rho_\mathrm{t}m_\mathrm{e}r_\mathrm{e}^2c^2z_\mathrm{p}^2\frac{Z_\mathrm{t}}{A_\mathrm{t}\beta^2}\ln\left(\frac{2m_\mathrm{e}\beta^2\gamma^2c^2}{I}-\beta^2\right), \quad (1)$$

where N_A is the Avogadro number, m_e and r_e are the mass and the classical radius of the electron, z_p is the nuclear charge of an incident particle, Z_t and A_t are the atomic number and the nuclear mass of the target, the residual gas density can be calculated by the state equation of ideal gas $\rho_\mathrm{t} = PA_\mathrm{t}/RT$ with gas pressure P, temperature T and ideal gas constant R, βc and γ are the velocity and the relativistic factor of the incident particle, I is the mean excitation/ionization potential of gas targets, β^2 inside the bracket represents a relativistic correction term. In the energy range of $0.05 \le \beta\gamma \le 1000$, the Bethe formula gives a good approximation to the energy loss of heavy particles within a few percent.

Some experimental data of the ionization energy for general residual gases are shown in Table 1 [6]. Subsequently, the energy loss from a single-beam particle traversing through gas targets can be calculated in Eq. (1) and by another well-known code named SRIM [7] as well. Substituting the beam parameters of Kr^{30+} with energy 422 MeV/u at 293.15 K and the main gas species of H_2 with 8×10^{-10} Pa pressure in HIRFL-CSRm. The calculated energy loss is 2.29×10^{-14} MeV/mm in Eq. (1), and 2.18×10^{-14} MeV/mm by the SRIM code.

The calculation results actually indicate that the energy loss transferred to the residual gas targets is actually negligible compared to the beam kinetic energy. In addition, the results of the two calculation methods will have less discrepancy when the incident particle is a light ion like the proton. The Bethe formula treats the incident particle as a bare nuclei with the atomic charge z_p by default, while the SRIM code uses an effective charge state instead. Generally, the energy loss of heavy ions calculated by the SRIM is quite identical to those experimental data within a mean error of 8.90% [7].

The energy loss for a single-beam particle traveling through residual gas targets is solved. Subsequently, the final signal photons reaching the camera chip can be approximately evaluated in Eq. (2).

$$N_\mathrm{d} = \frac{\mathrm{d}E}{\mathrm{d}x}\frac{L}{W_\mathrm{i}}N_\mathrm{p}MGFtf_\mathrm{r}, \quad (2)$$

where N_p means the number of beam particles per bunch, M is the magnification and transmission factor for the optics system, G is the gain of the MCPs, F means an average quantum efficiency of the phosphor screen and the

Table 1 Ionization energies for gases included in the air at 293.15 K, 1 atm [6], E_i means the primary ionization energy, I is the mean excitation/ionization energy and W_i is the effective energy to create an ion-electron pair

Gas species	E_i (eV)	I (eV)	W_i (eV)
H_2	15.4	19.2	37
N_2	16.7	85.0	35
O_2	12.8	95.0	31
H_2O	12.6	71.6	38
CO_2	13.8	85.9	34

camera chip, t is the integration/exposure time of the camera, $f_r = \beta c / C$ means the revolution frequency and $C = 161$ m is the circumference of HIRFL-CSRm.

Substituting the energy loss of 2.18×10^{-14} MeV/mm by the SRIM code, f_r and N_p are determined by the kinetic energy 422 MeV/u and the beam current 1.5 mA in the normal operation mode of HIRFL-CSRm; the two-layer MCPs with a "V" style channel combination are chosen for a high gain G of 10^6 and an effective length L of 30 mm; the phosphor screen and the camera chip totally attain an average quantum efficiency F around 50%, which actually varies with different photon wavelengths; the factor M relating to the solid angle and the lens material is roughly calculated approximately 10^{-3} for our optics system. Eventually, the total photon yield arriving at the camera chip is approximately 2.05×10^3 only for a turn of the beam passage, and 2.76×10^7 for the camera exposure time of 10 ms, both of which are enough for the detectable sensitivity of the sCMOS chip used. As a result, though the residual gas pressure is extremely low as 8×10^{-10} Pa, the new IPM would successfully work at HIRFL-CSRm.

2.3 Some considerations about residual gas

In fact, the residual gas used for the IPM detection should be regarded as a compound gas target. The gas composition is excepted to be 85% of H_2, and 15% of N_2 or CO in HIRFL-CSR [1]. In this case, an accurate stopping power can be calculated by $S_c = \sum f_i S_i$, where f_i and S_i are the mass percentage and the stopping power of each element. Compared with the lightest gas species H_2, a heavier gas molecule will result in larger electric stopping power and consequently more ion-electron pairs acting as the IPM signals.

The residual gas pressure is positively proportional to the IPM signal amplitude, but it only slightly influences the beam width by changing the signal-to-noise ratio and the statistical error from the profile data. Compared with the camera exposure time, only a fast changing of the gas pressure can notably affect the beam size fitted by the IPM data. The most probable speed of ideal gas molecules based on a Maxwell-Boltzmann distribution is $v = \sqrt{2k_B T / \pi m}$, with molecular mass m, temperature T, and Boltzmann constant k_B. For an average nuclear mass of 18.7 for a compound gas target at 293.15 K, the velocity is calculated approximately 288 m/s. Consequently, the time it takes for molecules to reach a nearby pump is much longer than the ionization and capture events. Therefore, the global pressure may be considered constant with respect to the camera exposure time. As for the local pressure variation, the previous research indicates a parabolic pressure distribution between the two pumps surrounding an IPM. And the pressure difference between the pressure gauge and the IPM location is no larger than 7% [8].

The residual gas molecules depleted by the IPM also can be roughly assessed. Based on the state equation of ideal gas $n = pV/RT$, the detectable volume within the new IPM is approximately 648 cm^3 resulting in about 1.28×10^8 gas molecules capable of producing measurable particles. However, according to Eq. (2), the created residual gas ions is calculated approximately 5.52×10^4 for the camera exposure time of 10 ms, being only 0.043% of the total gas molecules inside the IPM working volume. Furthermore, the gas molecules actually can be supplemented by the beam-induced desorption from the pipe walls [8]. Unfortunately, the precise measurements for both the local pressure variation and the residual gas depletion cannot be done at the HIRFL-CSRm IPM site.

2.4 Space charge and initial momentum analysis

Three major factors still could negatively affect the IPM measurement accuracy, which are the initial velocity of signal particles, the non-uniformity of the electric field and the space charge field from intense beams. In theory, the most of the energy transfer goes into the electrons since the electron mass is small. Therefore, the initial velocity of gas ions mainly appears as the thermal motion of gas molecules and it hardly causes the position deviation during the whole drift journey. For a non-uniform beam distribution in HIRFL-CSRm, the impact of the space charge field on the signal gas ions can be approximatively calculated in Eq. (3) [9].

$$E_{em} = \frac{I_B}{2\pi\varepsilon_0 \beta c \gamma^2} \cdot \frac{1}{r} \left(1 - e^{-r^2/2\sigma^2}\right), \tag{3}$$

where I_B is the beam current, ε_0 is the vacuum permittivity, σ is the rms size for a Gaussian distribution beam, and r represents the distance from the beam center. Substituting the cooled beam parameters of Kr^{30+} with energy 422 MeV/u, current 1.5 mA and $\sigma = 1$ mm, E_{em} calculated at $r = \sqrt{2}\sigma$ shows a relatively large value of 26.38 V/m. The potential difference of 6 kV between a 120 mm clearance attains a field strength around 5×10^4 V/m. Thus, the space charge field is actually negligible compared to the electric field under the HIRFL-CSRm beam conditions.

Additionally, a systematic simulation integrating the initial momentum and the space charge effect can be done by some laboratory-developed codes [10]. The upper panel of Fig. 3 shows a space charge field E_x as a function of the horizontal position. The value of $|E_x|$ reaches 28 V/m at maximum, which agrees well with the calculation result in Eq. (3).

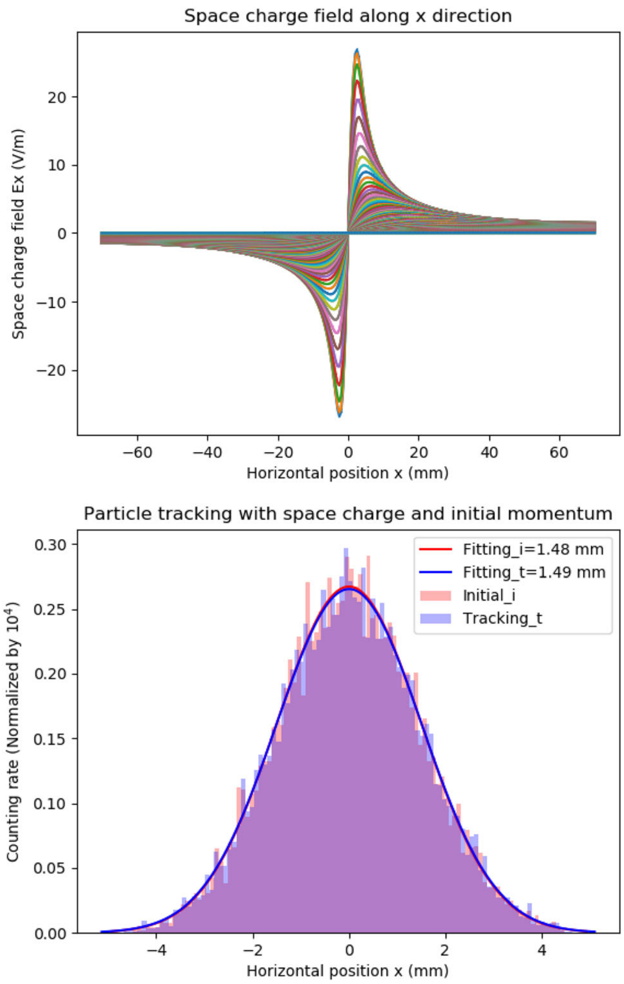

Fig. 3 (Color online) IPM Simulations by a laboratory-developed code named IPMsim3D [10]. The upper panel depicts a space charge field E_x as a function of the horizontal position. The value of $|E_x|$ reaches 28 V/m at maximum. The lower panel shows the initial and tracked particles' counting rate as a function of the horizontal position. The fitted profile sizes are $\sigma_r = 1.49\,\mathrm{mm}$ for the initial particles and $\sigma_t = 1.48\,\mathrm{mm}$ for the tracked particles, respectively

The lower panel of Fig. 3 shows the initial and tracked particles' counting rate as a function of the horizontal position. The fitted profile sizes are $\sigma_i = 1.49\,\mathrm{mm}$ for the initial particles and $\sigma_\mathrm{t} = 1.48\,\mathrm{mm}$ for the tracked particles, respectively. The particle-tracking simulation indicates a broadening profile measurement error of $+0.68\%$ caused by the space charge of beams and the initial momentum of signal particles.

2.5 Simulations and beam experiments about electric field

It turns out that the major inaccuracy of the IPM profile measurement is caused by the electric field non-uniformity. Some commercial codes are capable of evaluating the field distribution and performing particle-tracking simulations. It is also feasible to import the three-dimensional field data into the laboratory-developed code [10] for an overall assessment.

In fact due to the presence of gaps and holes in the IPM structure, the real field distribution even varies with different high voltage (HV) settings. It is reasonable that different HV values applied on the IPM electrodes results in a small change of the field shape. Now IPMs in the world are mainly set with two HV types on the upper and lower plates: symmetric bipolar HV setting ($\pm 5\,\mathrm{kV}$ for example) and asymmetric unipolar HV setting (10 kV and ground level for example).

In order to explore the impact of different HV settings on the IPM properties, both commercial code simulations and beam experiments are done under three different HV setups shown in Table 2. Five critical IPM electrodes shown in Fig. 2 are set with different voltage combinations. Compared with the potential difference of 6 kV in the HV setup B and C, the setup A has a smaller value of 4 kV just in consideration of a redundant protection for the MCPs.

Figure 4 presents the field distributions simulated by a commercial code using the finite integration technique. Firstly, the electric field near the metallic chamber surface is reasonably distorted to satisfy the electric boundary condition. The equipotential lines in the upper panel of setup A are actually quite straight inside the IPM central region, which indicates a very flat and uniform vertical field E_y there. Near the MCPs area, the equipotential lines are deformed due to the mechanical breach and gaps. As a result, this curved shape of the electric field probably enlarges the profile projection on the sensor of IPM. By comparison, the lower panel of setup C shows an inversely curved field along all the drift path of signal particles, which most likely shrinks the signal ions' footprint on the MCPs. The electric field of setup B is not shown here, because it is very similar to that of the setup C (less curved).

Figure 5 shows the particle-tracking simulations under different HV settings shown in Table 2. An obvious linearity between the initial and detected particles' position has been found for all the three HV setups, which actually means a constant field distortion along the horizontal direction (x). In addition, a good field consistency in the longitudinal (z) and vertical (y) directions is also validated by changing the initial particle's coordinate along the two directions. The data slope of three tracking results reveal that the HV setup A has a broadening profile measurement error of $+1.50\%$, which probably results from the specific and curved field near the MCPs, also see the upper panel of Fig. 4. The setup B and C reflect a focusing error of -7.50% and -15.60% respectively, because both fields

Table 2 Three different HV setups applied on five crucial components for evaluating the IPM properties (unit: kV)

Setup	Upper plate	Lower plate	Upper MCP	Lower MCP	P46
A	2	− 2	− 1.8	0	2.8
B	6	0	0	1.8	4.6
C	6	0	− 1.8	0	2.8

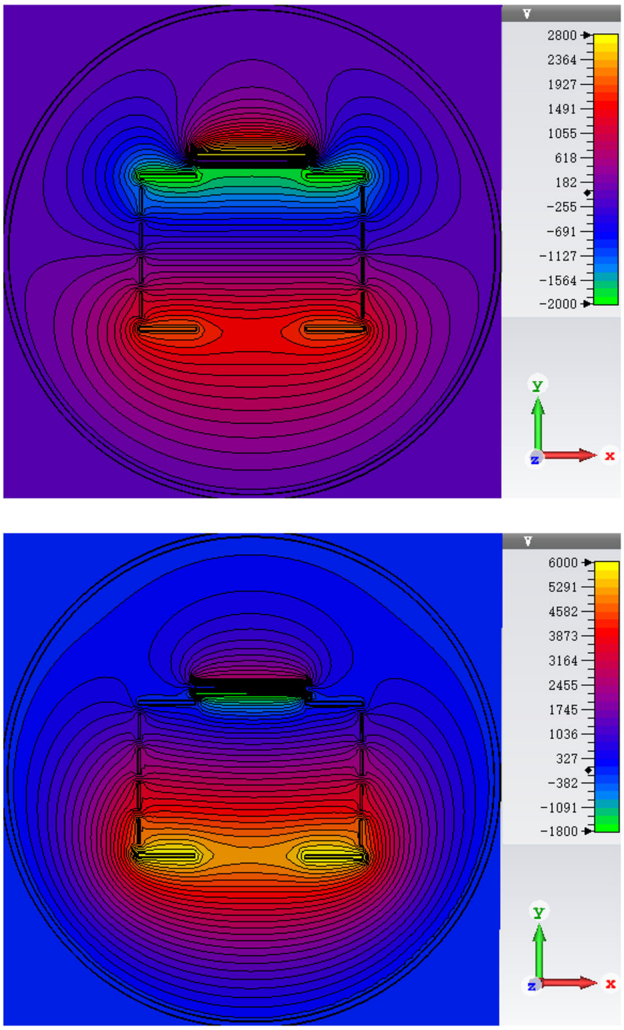

Fig. 4 (Color online) The electric field distribution as a function of different HV setups. The upper panel of setup A shows that the equipotential lines are quite flat in the central region, but obviously curved near the MCPs. The lower panel of setup C shows an inversely curved field inside all the IPM working region. The field distribution of setup B is not shown here, because it is very similar to that of the setup C (less curved)

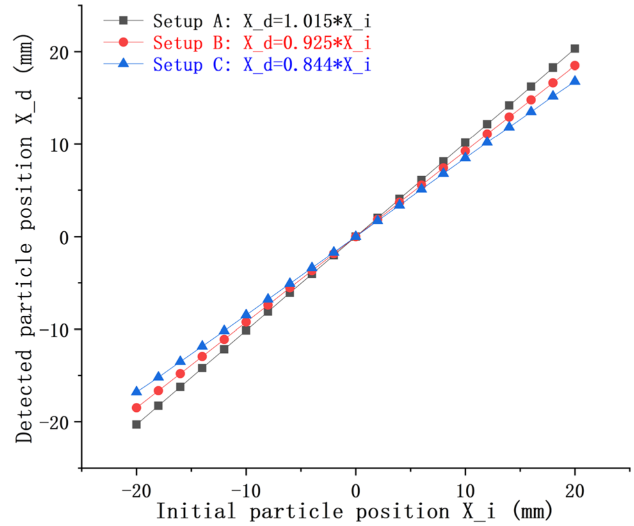

Fig. 5 (Color online) The tracked particle position as a function of the initial particle position. The setup A shows that the tacked particle position is a little larger than that of the initial, having a small and broadening error of $+1.50\%$. However, the setup B and C indicate a focusing error of -7.50% and -15.60%, respectively

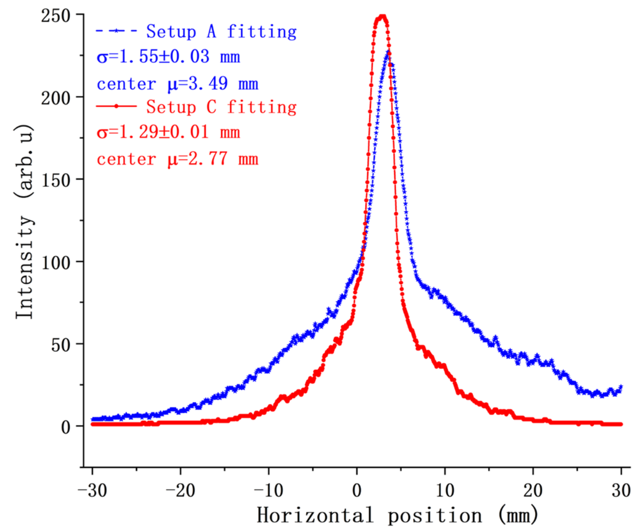

Fig. 6 (Color online) Intensity as a function of the horizontal position. The setup C apparently measures a smaller beam size and the measured beam center is closer to the geometric center compared to that of the setup A. The profile data of setup B is not shown due to its strange asymmetric distribution in the longitudinal direction, details see the next subsection

show an inversely curved shape compared to that of the setup A.

Figure 6 depicts two obvious bi-Gaussian profiles for the beams cooled enough to reach an equilibrium state in HIRFL-CSRm. In theory, the smallest transverse emittance should stay unchanged under the same cooling condition. As shown in Eq. (4), this ultimate beam size is mainly determined by the tune shift resulting from the increase of the space charge during the beam cooling [11].

$$\sigma_x = \sqrt{\epsilon_x \beta_x} = \sqrt{\frac{N R r_i \beta_x}{\pi l_b \beta^2 \gamma^3 \Delta \nu}} \quad (4)$$

where β_x is the transverse betatron function, $N = I/(Zef_r)$ means the number of beam particles per bunch, $l_b = C/(2\sqrt{\pi})$ and $R = C/(2\pi)$ with the circumference of $C = 161$ m, $r_i = (Ze)^2/AM$ is the classical ion radius, the experimental data of $\Delta\nu = 0.1$–0.2 [11] means the maximum tune shift caused by the beam cooling. Substituting the injected beam parameters of Kr^{28+} with energy 4.98 MeV/u, current 125 μA and $\beta_x = 15$ mm at the new IPM site, eventually an equilibrium beam size is calculated $\sigma_x = 1.62$–2.29 mm. This rough calculation gives a possible range for the cooled beam size in HIRFL-CSRm as a theoretical benchmark.

Figure 6 shows that the new IPM indeed measures two different beam profiles as a consequence of different HV settings. This can only be explained that the electric field of the HV setup C focuses the signal ions more strongly than that of the setup A. And this focusing field even moves the whole signal ions' projection to the geometric center of the new IPM. Apparently, the beam size of setup C is smaller than that of the setup A with a relative error of -16.68%, which is quite identical to the simulated error difference of -17.10% shown in Fig. 5. The profile measurements show a very good agreement with the simulations of the commercial software. Consequently, some data corrections could be added to precisely retrieve the real beam size and it is particularly necessary for the IPM applications in intense beams.

The former vertical IPM has been benchmarked with a wire scanner in SSC-Linac, and it measures a beam size approximately 8.8% smaller than that of the wire scanner [4]. This measurement error mainly comes from the deformity of the electric field, because the space charge effect there is also negligible and the profile measurements are very identical to the field simulations. Unfortunately due to the space limitation at HIRFL-CSRm, the new horizontal IPM cannot be checked by another profile instrument.

In conclusion, the symmetric HV setup A achieves more uniform field distribution compared to asymmetric ones like the setup B and C, but it brings more challenges for the MCPs' insulation and operation, especially for the IPM applications under the ultra-high voltage setup.

2.6 Operational cautions and experimental anomalies

One unusual phenomenon should be paid attention to during the IPM operation. When the two-layer MCPs are supplied with the same polarity HV channels, the lower MCP will be affected by some induced voltages and consequently the voltage feedback reading is always improper. As a result, the gain of the MCPs becomes much lower than the value expected and the risk of discharging between the two MCPs also rises. This problem possibly results from the HV board defect or the unreal high resistance between the two MCPs. And fortunately, it can be avoided by using the opposite polarity channels for the two-layer MCPs.

Another unexpected behavior of the phosphor screen flashing during the beam operation happened only once at HIRFL-CSRm. With the aid of an interceptive scintillator screen, the reason for this anomaly is excluded for the P46 defect and eventually it is found to be a small malfunction of the magnet current.

Also as shown in Fig. 7, the new IPM measures an asymmetric profile distribution along the longitudinal direction, but the simulations show no evidence to explain it. A similar phenomenon also occurred in the Jülich IPM [12], and the cause was deduced to be the defect of the phosphor screen. During our IPM experiments, this anomaly disappears and even repeats again as long as the IPM voltages change between the setup B and C. Therefore, this phenomenon probably results from the zero potential difference between the lower plate and the upper MCP. Most likely, it is the improper HV setting making the MCPs vulnerable for the secondary particles' impact or possible partial field deformity forming. More experiments are needed to further study this issue.

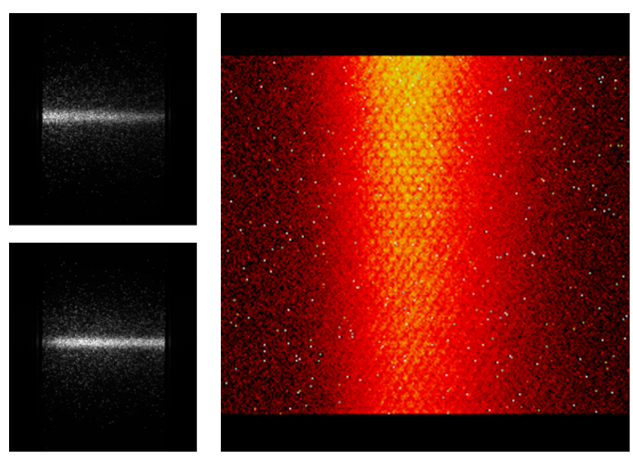

Fig. 7 (Color online) Raw profile images observed by the IPMs. The left upper panel of setup B shows an asymmetric profile along the longitudinal direction, while the left lower panel of setup C obtains a normal profile distribution. The right panel from the Jülich IPM also presents a similar asymmetry [12]. The raw image of setup A is not shown here because it is very similar to that of the setup C. In all pictures, the light extension orientation is exactly the longitudinal direction of the beam propagation

3 Transverse electron cooling study

On each ring of HIRFL, an electron cooler is deployed to provide high-quality beams for all sorts of experimental applications. Previously in HIRFL-CSR, the transverse beam cooling can only be qualitatively analyzed by the spectrum sidebands of a Schottky pickup [13], because this method demands a precise assessment for the pickup's transverse transfer impedance. However, some crucial parameters of the electron cooling require a precise profile measurement for further optimizations, such as the anode voltage of the electron gun, the injected electron pulse length and so on. More information about the electron cooling experiments in HIRFL-CSR can be seen in reference [14].

Figure 8 illustrates the profile distributions as a function of different elapsed times after 3 and 33 bunches injected. The beams with only 3 bunches injection barely accumulate in HIRFL-CSRm without the electron cooling. However, the IPM can still measure the weak profile signal as a small bump over the background noise, which indicates a high sensitivity for the IPM applications in low beam currents. The beam profiles after 33 bunches injection show a similar distribution as a function of time, while the signal amplitude obtained at 1700 ms is apparently smaller than that at 340 ms. It seems possible to use an IPM for the beam lifetime measurement in a synchrotron, as long as a precise calibration between the signal amplitude and the beam current can be done.

Figure 9 presents the beam size variation as a function of the elapsed time under different anode voltages. Apparently, the beam width with an anode voltage of 400 V will still narrow down, showing an obvious linear trend at the end of 2.15 s. As a result, the beams are not cooled enough during the IPM measurements. The beam sizes with the anode voltage of 600 V and 800 V finally become equal in the fifth frame data at 2.15 s. However referring to the former profile data, there is no doubt that the beams with the anode voltage of 800 V achieve a stronger cooling power than that of 600 V.

Figure 10 shows the beam size variation as a function of the elapsed time under different electron pulse lengths. The beam widths with the electron pulse length of 300 ns and 400 ns still keep a decreasing tendency at the end of 2.23 s, indicating a relatively weak cooling power. Both beams with the 600 ns and 1200 ns electron pulse length are almost cooled enough from the second frame data at 0.89 s, but we can still distinguish a stronger cooling power

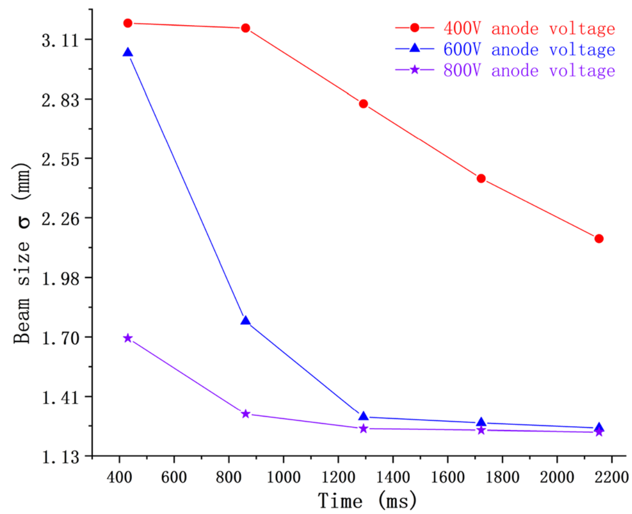

Fig. 9 (Color online) Beam size as a function of the elapsed time. The beam width variation under different anode voltages with the 400 ns electron pulse length setting at HIRFL-CSRm

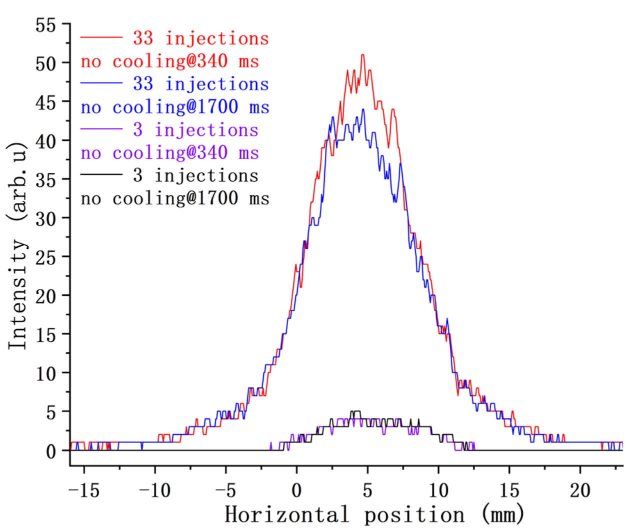

Fig. 8 (Color online) Beam profile as a function of different elapsed times. The profile distribution variation after 3 and 33 bunches injected without the electron cooling at HIRFL-CSRm

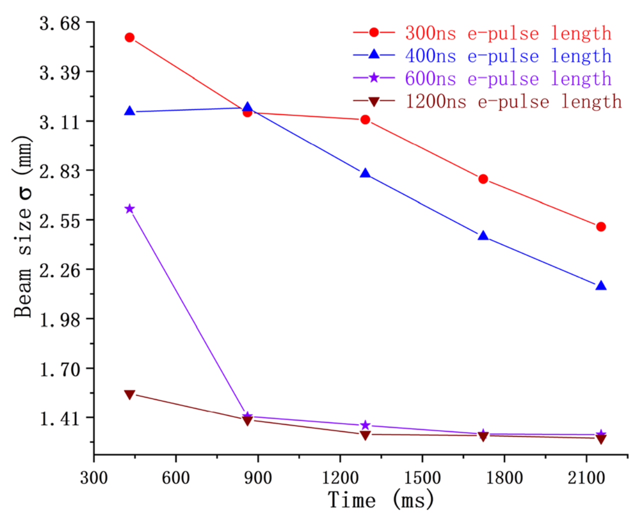

Fig. 10 (Color online) Beam size as a function of the elapsed time. The beam width variation under different electron pulse lengths with the 400 V anode voltage setting at HIRFL-CSRm

coming from the 1200 ns setting by the first frame data at 0.45 s. The profile measurements also confirm the existence of an equilibrium state for the cooled beams in HIRFL-CSRm.

Figure 11 directly displays the beam profile variation as a function of time under different cooling settings. The upper left and right panels clearly reveal a proportional relation between the anode voltage and the cooling power. Also, the lower left and right panels show that a longer electron pulse length results in a stronger cooling power. In conclusion, within certain range the profile measurements directly express a positive correlation between the cooling parameters and the cooling power.

4 Orbit oscillation in normal operation mode

HIRFL-CSR is a double-ring system. In every operation cycle, the stable-nucleus beams from the injectors are accumulated, cooled and accelerated in CSRm, then extracted fast to CSRe. The accumulation duration of CSRm is around 10 s. Considering the ramping rate of the magnetic field in dipole magnets to be 0.1–0.4 T/s, the acceleration time of CSRm will be nearly 3 s. As a result, the operation cycle is approximately 17 s [1].

The horizontal IPM is set to be triggered by a nearby DCCT for synchronously saving the beam profile and current data. Depending on the trigger threshold and the response time, the IPM nearly measures 36 frames profile data during the whole normal operation mode. In the left panel of Fig. 12, the profile measurements clearly show a whole cycle period around 16.45 s, which consists of an accumulation time of 0–10 s, an acceleration process of 10–14.6 s, following with 2 s for the magnetic field stay, then extracted fast into CSRe.

The right panel of Fig. 12 shows the horizontal orbit data as a function of time. During the accumulation time of 0-10 s, the beam current represented by the DCCT value increases steadily up to 0.19 mA because of the sequential multi-turn injection (MTI) process. The beam size only

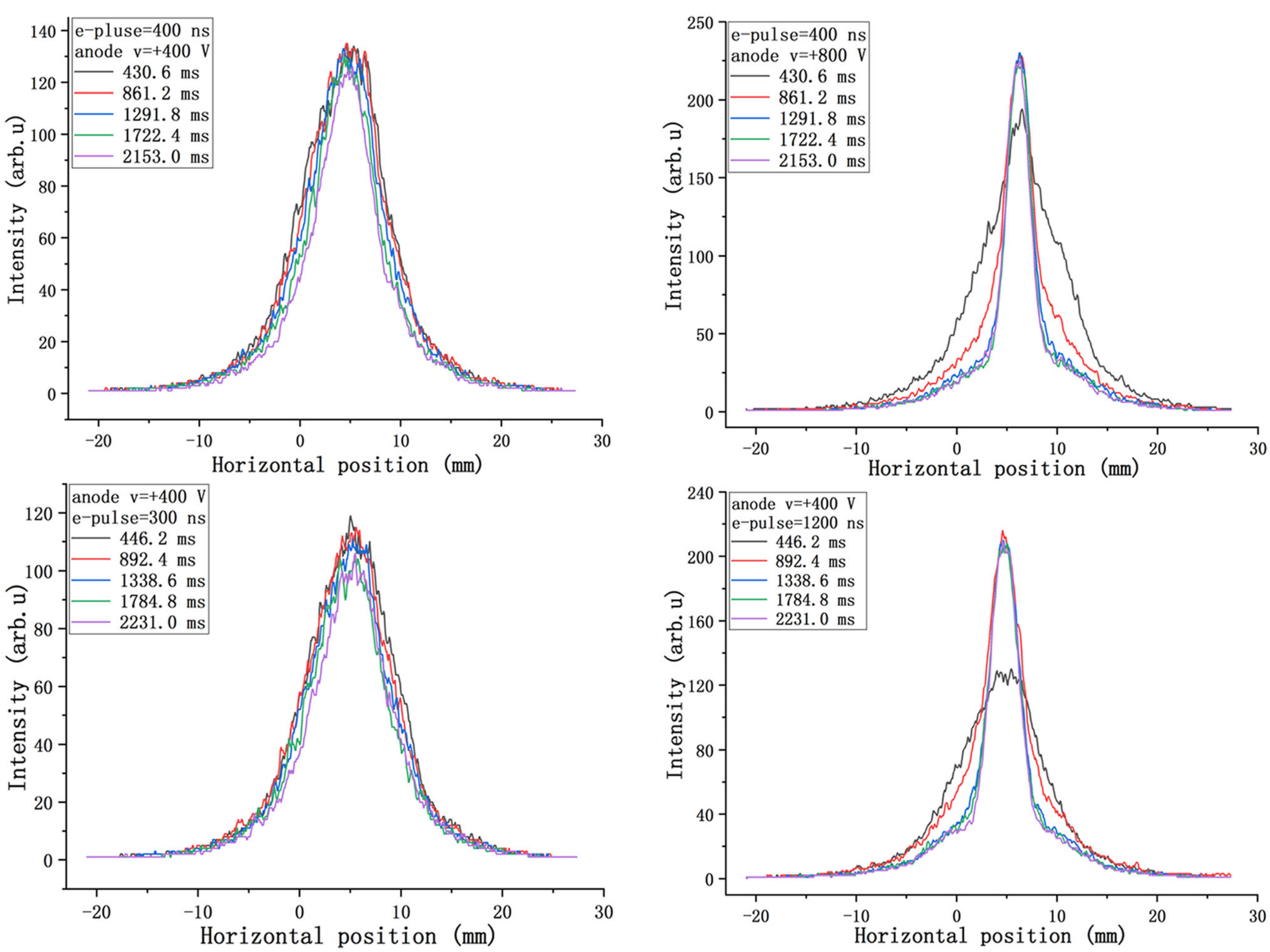

Fig. 11 (Color online) Beam profile as a function of time under different cooling setups. The upper left and right panels show the influence of different anode voltages, and the lower left and right panels present the impact of different electron pulse lengths on the cooling power

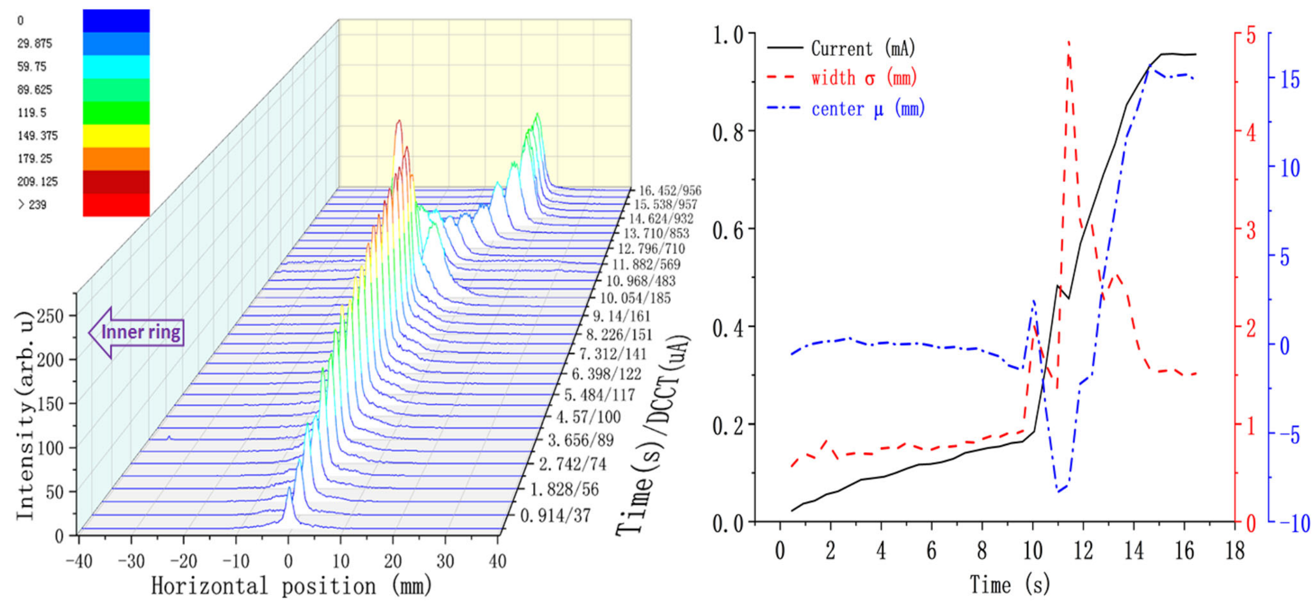

Fig. 12 (Color online) Beam orbit oscillation as a function of time. The left panel displays the beam orbit oscillation during the normal operation mode of HIRFL-CSRm. The right panel detailedly shows that the beam current is dramatically increasing during the acceleration process, whereas both the beam size and the mean position undergo a non-monotonous changing at that time

changes slightly and the mean position almost stays the same, because the emittance growth due to the MTI process in the horizontal phase space is of course much smaller than the increase of the beam particles.

In the acceleration process of 10 to 14.6 s, both the beam size and the mean position undergo a large oscillation. A large beam displacement of more than 25 mm mainly results from the mismatch between the magnetic field ramping and the particles' momentum increasing. The beam size firstly increases fast up to the maximum σ of 5 mm and then decreases to a stable value around 1.5 mm. This non-monotonous oscillation only can be ambiguously attributed to the betatron function variation, the momentum spread and dispersion contribution, or the possible mismatch between the electron cooling and the energy ramping at HIRFL-CSRm. Some similar emittance growth research during the energy ramping actually implies a main cause of non-monotonous betatron function changing [15].

5 Discussion of injection mismatch and IPM's prospects

The injection mismatch causes the transverse emittance blow-up and consequently becomes one of vital barriers for the beam brightness upgrade in a synchrotron and collider. The horizontal beam motion is often influenced by the dispersion due to the existence of dipole magnets, thus the normalized emittance can be expressed in Eq. (5).

$$\epsilon_{nx} = \left(\frac{\sigma_x^2}{\beta_x} - \frac{(D_x \Delta p/p)^2}{\beta_x}\right)\beta\gamma \tag{5}$$

where ϵ_{nx} means the normalized emittance, D_x and $\Delta p/p$ are the dispersion and the momentum spread, respectively. There is no doubt that the betatron function and dispersion mismatches are two of major sources for the emittance blow-up.

Figure 13 is an illustration to well explain the mismatch analysis using the turn-by-turn profile measurements by a fast wire scanner [16], which shows an obvious emittance growth as a function of turn numbers. As a contrast, a rematched injection optics apparently achieves less emittance increase and consequently higher beam quality. Turn-by-turn profiles are firstly analyzed by a Gaussian fitting, and both the beam size and mean position data possibly present a similar sinusoidal oscillation in the presence of the optics mismatch.

The trajectory's mean position is dominated by the momentum offset via dispersion with a small contribution from the closed orbit. The sinusoidal amplitude is attributed to the main contribution from dispersion mismatch and a small part due to the magnet mis-steering. Besides, the transverse displacement data can be further analyzed by the Fourier conversion to obtain the fractional tune value.

The beam width shows a similar oscillation behavior during the turn-by-turn profile measurements. It is mainly determined by the betatron and dispersion mismatches, and

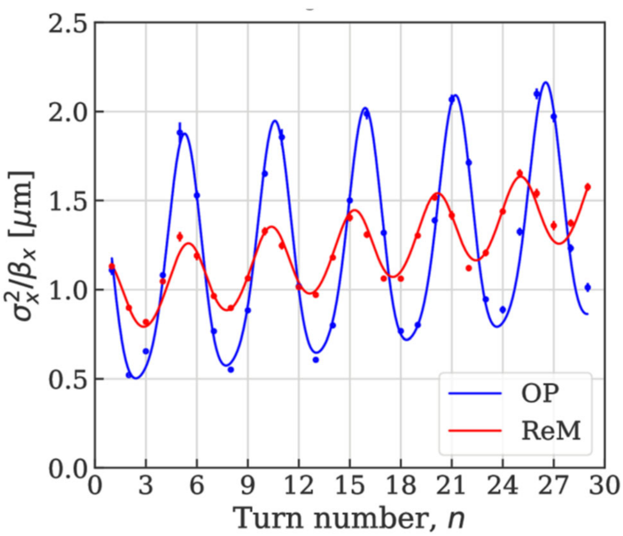

Fig. 13 (Color online) Turn-by-turn profile measurements under the Operational setup (OP) and the Rematched injection optics (ReM) [16]. Apparently a smaller emittance blow-up comes from the beams of ReM rather than that of OP

a small contribution from the beam scattering on wires as well. This scattering contribution to the emittance blow-up can be approximately evaluated in Eq. (6) [17].

$$\Delta\epsilon = \frac{f_r \beta_x r^2}{2 l v_{\mathrm{w}}} \left(\frac{13.6}{p\beta}\right)^2 \left[1 + 0.088 \log_{10}\left(\frac{r}{l}\right)\right]^2 \tag{6}$$

where $r \simeq \pi d/4$ is the average thickness of a cylindrical wire, l means the radial length of the wire, v_{w} represents the scanning velocity of the wire, The constants 13.6 with the unit of MeV and 0.088 are called Highland constants, details see [18]. A single-beam passage only causes small angle deflection due to the wires' scattering, but multi-turn measurements can accumulate a noticeable emittance blow-up.

At the same time of the new IPM deployed in August 2018, the transverse emittance instruments were also installed at the injection line of HIRFL-CSRm, which comprise two sets of the slit and wire scanner systems. As shown in Fig. 14, the cylindrical tungsten wire has a diameter of 35 µm and the tantalum-copper slit is set a width of 0.2 mm. The distance between the slit and the wire scanner is 495 mm in the vertical direction and 480 mm for the horizontal orientation, respectively. The control panel is also built on an EPICS system to calculate the beam Twiss parameters online. This interceptive method is especially suitable for the relatively weak beams around 1 µA at the HIRFL-CSRm injector.

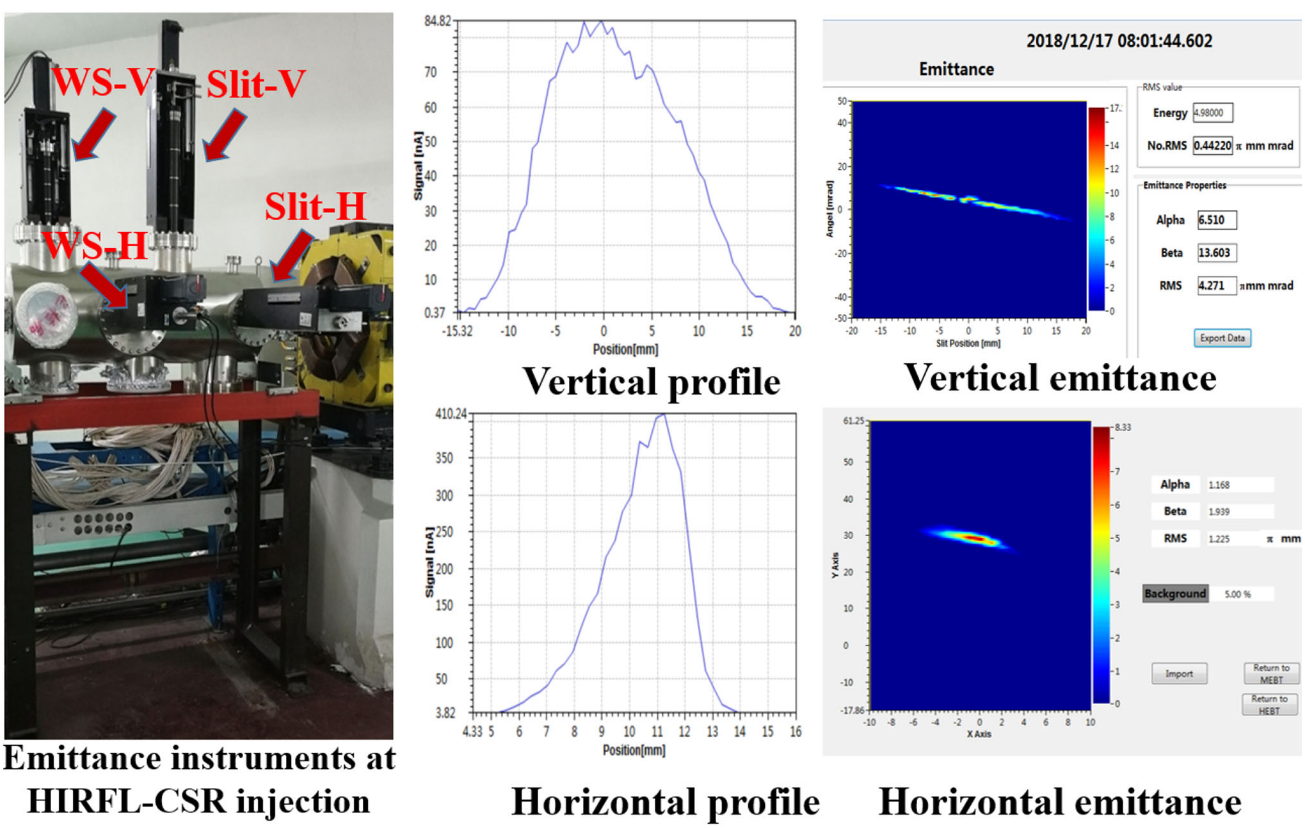

Fig. 14 (Color online) New transverse emittance instruments comprising two sets of the slit and wire scanner system at the HIRFL-CSRm injector. The illustrated emittance is measured under the beam parameters of Kr^{28+}, energy 4.98 MeV/u and current 1 µA

Presently, another type of IPM with the electron collection and a magnet for the space charge suppression is also under design for HIRFL-CSRm, and future High-Intensity Heavy Ion Accelerator Facility (HIAF) as well [19]. This IPM using the electric signal acquisition is fast enough to perform the turn-by-turn profile measurements. In cooperation with the transverse emittance instruments shown in Fig. 14, the fast IPM has great prospects for the injection mismatch study, as well as further measurements for the tune, dispersion and chromaticity without extra beam excitations and disturbances.

6 Summary

In August 2018, a new horizontal IPM was developed and deployed in HIRFL-CSRm with a compact mechanical design and an upgraded control system. All the major issues, detailed simulations and beam experiments were carried out to explain the design keys and to verify the IPM properties under different HV setups as well. Meanwhile, some operational cautions and experimental anomalies were found and studied, one of which is the profile behavior of an asymmetric distribution in the longitudinal direction. The reason for this asymmetry can only be deduced to the improper HV settings, and more experiments are needed to further study this issue.

Subsequently, the transverse beam cooling study has been done taking advantage of the new horizontal IPM, which clearly shows a positive relation between some crucial cooling parameters and the cooling power, such as the injected electron pulse length and the anode voltage of the electron gun. The new IPM has also measured the orbit oscillation during the normal operation mode of HIRFL-CSRm, and one of the interesting discoveries is the non-monotonous profile oscillation during the energy ramping. In the end, the transverse emittance blow-up and injection mismatches are discussed by using the turn-by-turn profile measurements. This non-destructive profile instrument also has great prospects for the tune, dispersion and chromaticity diagnostics in the proton and heavy ion synchrotron.

References

1. J.W. Xia, W.L. Zhan, B.W. Wei et al., The heavy ion cooler-storage-ring project (HIRFL-CSR) at Lanzhou. Nucl. Instrum. Methods A **488**, 11–25 (2002). https://doi.org/10.1016/S0168-9002(02)00475-8
2. T. Giacomini, S. Barabin, P. Forck et al., Development of Residual Gas Profile monitors at GSI. Am. Inst. Phys. Conf. Proc. **732**, 286–293 (2004). https://doi.org/10.1063/1.1831159
3. D. Bodart, B. Dehning, S. Levasseur et al., Development of an Ionization Profile Monitor based on a pixel detector for the CERN Proton Synchrotron, in *Proceedings of IBIC 2015*, Melbourne, Australia (2015)
4. H.M. Xie, J.X. Wu, L.J. Mao et al., A residual gas ionization profile monitor developed for HIRFL-CSR. Nucl. Phys. Rev. **34**, 773–778 (2017). https://doi.org/10.11804/NuclPhysRev.34.04.773
5. H.A. Bethe, Zur Theorie des Durchgangs schneller Korpuskularstrahlen durch Materie. Annalen der Physik **397**, 325–400 (1930). https://doi.org/10.1002/andp.19303970303
6. M. Tanabashi et al. (Particle Data Group), Review of particle physics. Phys. Rev. D **98**, 030001 (2018). https://doi.org/10.1103/PhysRevD.98.030001
7. J.F. Ziegler, M.D. Ziegler, J.P. Biersack, SRIM—the stopping and range of ions in matter (2010). Nucl. Instrum. Methods B **268**, 1818–1823 (2010). https://doi.org/10.1016/j.nimb.2010.02.091
8. D.A. Bartkoski, Analysis, prototyping, and design of an Ionization Profile Monitor for the Spallation Neutron Source Accumulator Ring. Doctoral dissertation in Knoxville, The University of Tennessee (2013)
9. K. Schindl, Space charge. Beam Meas. (1999). https://doi.org/10.1142/9789812818003_0004
10. M. Sapinski, P. Forck, T. Giacomini et al., Ionization profile monitor simulations—status and future plans, in *Proceedings of IBIC 2016*, Barcelona, Spain (2016). https://doi.org/10.18429/JACoW-IBIC2016-TUPG71
11. V.V. Parkhomchuk, A.N. Skrinsk, Electron cooling: 35 years of development. Physics Uspekhi **43**(5), 433–452 (2000). https://doi.org/10.1070/PU2000v043n05ABEH0007411
12. C. Böhme, I. Bekman, K. Reimers et al., Operational experience with the ionization beam profile monitor at COSY, in IPM 3rd Workshop Presentation, J-Parc, Japan (2018). https://doi.org/10.1023/A:1026053231074
13. F. Casper, Schottky signals for longitudinal and transverse bunched-beam diagnostics, CERN Accelerator School lecture, Dourdan, France (2008). https://doi.org/10.5170/CERN-2009-005.407
14. L.J. Mao, X.D. Yang, J. Li et al., Electron cooling experiments at HIRFL-CSR, in Proceedings of SAP 2014, Lanzhou, China, (2014)
15. M. Kuhn, Transverse emittance measurement and preservation at the LHC, CERN-THESIS-2016-149, Ph.D thesis, Humburg University (2016)
16. M.A. Fraser, Y. Dutheil, V. Forte et al., Matching studies between CERN PSB and PS through multi-turn beam profile acquisitions, in Proceedings of IPAC 2019, Melbourne, Australia (2019)
17. A.S. García, S.C.P. Albright, H. Bartosik et al., Systematic studies of transverse emittance measurements along the CERN PS Booster Cycle, in Proceedings of IPAC 2018, Vancouver, Canada (2018) https://doi.org/10.18429/JACoW-IPAC2018-TUPAF047
18. G.R. Lynch, O.I. Dahl, Approximations to multiple Coulomb scattering. Nucl. Instrum. Methods B **58**(1), 610 (1991). https://doi.org/10.1016/0168-583X(91)95671-Y
19. J.C. Yang, J.W. Xia, G.Q. Xiao et al., High Intensity heavy ion Accelerator Facility (HIAF) in China. Nucl. Instrum. Methods B **317**, 263–265 (2013). https://doi.org/10.1016/j.nimb.2013.08.046